Monthly Notices
of the
ROYAL ASTRONOMICAL SOCIETY

MNRAS **511,** 3138–3149 (2022)
Advance Access publication 2022 February 2

https://doi.org/10.1093/mnras/stac234

Multi-wavelength constraints on the outflow properties of the extremely bright millisecond radio bursts from the galactic magnetar SGR 1935 + 2154

Shotaro Yamasaki ,[1★] Kazumi Kashiyama[2,3] and Kohta Murase [4,5,6,7]

[1] *Racah Institute of Physics, The Hebrew University of Jerusalem, Jerusalem 91904, Israel*
[2] *Department of Physics, School of Science, The University of Tokyo, 7-3-1 Hongo, Bunkyo-ku, Tokyo 113-0033, Japan*
[3] *Research Center for the Early Universe, School of Science, The University of Tokyo, 7-3-1 Hongo, Bunkyo-ku, Tokyo 113-0033, Japan*
[4] *Department of Physics, The Pennsylvania State University, University Park, Pennsylvania 16802, USA*
[5] *Department of Astronomy & Astrophysics, The Pennsylvania State University, University Park, Pennsylvania 16802, USA*
[6] *Center for Multimessenger Astrophysics, Institute for Gravitation and the Cosmos, The Pennsylvania State University, University Park, Pennsylvania 16802, USA*
[7] *Center for Gravitational Physics, Yukawa Institute for Theoretical Physics, Kyoto, Kyoto 606-8502 Japan*

Accepted 2022 January 24. Received 2022 January 24; in original form 2021 September 23

ABSTRACT

Extremely bright coherent radio bursts with millisecond duration, reminiscent of cosmological fast radio bursts, were codetected with anomalously-hard X-ray bursts from a Galactic magnetar SGR 1935 + 2154. We investigate the possibility that the event was triggered by the magnetic energy injection inside the magnetosphere, thereby producing magnetically-trapped fireball (FB) and relativistic outflows simultaneously. The thermal component of the X-ray burst is consistent with a trapped FB with an average temperature of ∼200–300 keV and size of $\sim 10^5$ cm. Meanwhile, the non-thermal component of the X-ray burst and the coherent radio burst may arise from relativistic outflows. We calculate the dynamical evolution of the outflow, launched with an energy budget of 10^{39}–10^{40} erg comparable to that for the trapped FB, for different initial baryon load η and magnetization σ_0. If hard X-ray and radio bursts are both produced by the energy dissipation of the outflow, the outflow properties are constrained by combining the conditions for photon escape and the intrinsic timing offset $\lesssim 10$ ms among radio and X-ray burst spikes. We show that the hard X-ray burst must be generated at $r_{\rm X} \gtrsim 10^8$ cm from the magnetar, irrespective of the emission mechanism. Moreover, we find that the outflow quickly accelerates up to a Lorentz factor of $10^2 \lesssim \Gamma \lesssim 10^3$ by the time it reaches the edge of the magnetosphere and the dissipation occurs at $10^{12}\ {\rm cm} \lesssim r_{\rm radio,\,X} \lesssim 10^{14}$ cm. Our results imply either extremely-clean ($\eta \gtrsim 10^4$) or highly-magnetized ($\sigma_0 \gtrsim 10^3$) outflows, which might be consistent with the rarity of the phenomenon.

Key words: stars: magnetars – stars: neutron.

1 INTRODUCTION

Recently, one of the most prolific transient magnetars, SGR J1935 + 2154 (Israel et al. 2016) went into an intense bursting episode on 2020 April 27 , and hundreds of X-ray bursts were recorded in a few hours (Borghese et al. 2020; Younes et al. 2021). During this active phase, an extremely intense radio burst with millisecond duration, reminiscent of cosmological fast radio bursts (FRBs), was detected by radio telescopes CHIME/FRB (CHIME/FRB Collaboration 2020) and STARE2 (Bochenek et al. 2020) on 2022 April 28, strengthening the connection between FRBs and magnetars. Importantly, Insight/HXMT (Li et al. 2021a), Konus-Wind (Ridnaia et al. 2021), INTEGRAL/IBIS (Mereghetti et al. 2020), and AGILE (Tavani et al. 2021) independently detected an X-ray burst associated with the FRB-like radio burst (Mereghetti et al. 2020; Li et al. 2021a; Ridnaia et al. 2021; Tavani et al. 2021); the timing of the emissions is the same within the observational uncertainties and the radio burst detected by CHIME have a similar temporal structure to the X-ray burst. The X-ray burst is peculiar in that the spectrum is much harder than a typical SGR burst with comparable (or even higher) fluences and FRBs were not detected with many other X-ray bursts from the same source (Lin et al. 2020).

Theoretical interpretations of the April 28 event are broadly classified into two categories: ‘close-in’ and ‘far-away’ scenarios, depending on how close the radio emission is generated from the central engine (i.e. the magnetar). The former includes the curvature radiation in the open magnetic fields (e.g. Lu, Kumar & Zhang 2020; Katz 2020; Yang & Zhang 2021), the plasma instability triggered by magnetic reconnection (Lyutikov & Popov 2020; Lyutikov 2020) and the low-altitude magnetospheric emission (Wadiasingh & Timokhin 2019; Wadiasingh & Chirenti 2020), whereas the latter invokes a maser-type instability at the shock between magnetar flare wind and the pre-existing material (e.g. Margalit et al. 2020; Yuan et al. 2020; Yu et al. 2021). The possibilities of generating double/multiple-peaked radio pulses by the quasi-periodic oscillation of magnetars (Wang 2020) or the scintillation effect (Simard & Ravi 2020) are also discussed. Whether the April 28 event as well as cosmological FRBs

★ E-mail: shotaro.s.yamasaki@gmail.com

are generated by close-in or far-away models is subject to intense debate in the community, both from observational and theoretical aspects. Regarding cosmological FRBs, recent FAST observations on varying polarization angles in some repeaters (Luo et al. 2020) and discovery of recurrent bursts from FRB 121102 with too short separations down to milliseconds and too large energy budget (Li et al. 2021b) to accommodate the far-away (maser-type) models may prefer close-in (curvature-type) models. Meanwhile, it has also been pointed out that close-in models could have some theoretical flaws because realistic plasma effects are often neglected (e.g. Lyubarsky 2021).

In either the close-in and far-away models, the event is triggered by a deposition of magnetic energy in the magnetosphere, which may results in the formation of an electron/positron ($e^{\pm}$) plasma bubble confined to the stellar surface by the strong magnetic pressure (Thompson & Duncan 1995, 1996), so-called trapped fireball (FB), and also launching an outflow of relativistic plasma (or an expanding FB). In this paper, we aim to put general constraints on such FBs (i.e. the properties of the outflow responsible for the X-ray and/or radio bursts) with modest assumptions on the radiation mechanism, based on the multi-wavelength observations of the April 28 event. While the thermal component of the X-ray burst is consistent with a trapped FB, the non-thermal component of the X-ray burst and the coherent radio burst may arise from relativistic outflows. Regarding the origins of hard X-ray burst, we examine the two possibilities that (1) it is produced in the vicinity of the NS or the trapped FB (Section 3.1) and that (2) it arises from the relativistic outflow (Section 4.2). The second possibility is investigated by considering the evolution of outflows with different properties, assuming that the hard X-ray and coherent radio bursts have been produced due to some sort of energy dissipation inside the outflows, which broadly includes far-away models.

This paper is organized as follows. In Section 2, we summarize the key observational properties of the April 28 event. We constrain the total energy budget of the event in Section 3.1 by assuming that the thermal component of the X-ray spectrum is due to the trapped FB. In Section 3.2, we calculate the dynamical evolution of the outflow, which is likely responsible for the FRB-like burst and the non-thermal part of the hard X-ray burst spectrum. Constraints on the outflow properties are set from the general conditions required to generate the emission in Section 4 and our findings are summarized and implications are discussed in Section 5. Hereafter, we use $Q_x \equiv Q/10^x$ in cgs units.

2 KEY OBSERVED PROPERTIES OF APRIL 28 EVENTS FROM SGR 1935 + 2154

Here, we review the key observed properties of the radio and X-ray bursts from SGR 1935 + 2154 on 2020 May 28 (see also Table 1).

SGR 1935 + 2154

SGR 1935 + 2154 is one of the most prolific transient magnetars; the spin period and the spin-down rate are measured to be $P_{\rm spin} = 3.24$ s and $\dot{P} = 1.43 \times 10^{-11}\,{\rm s\,s^{-1}}$, respectively (Israel et al. 2016). Accordingly, the surface dipole magnetic field strength is estimated as $B_{\rm p} = 2.2 \times 10^{14}$ G. This magnetar has been recently in an active phase since 2020 April 27 (Younes et al. 2021). The distance estimate is somewhat uncertain. SGR 1935 + 2154 is spatially associated with the supernova remnant (SNR) G57.2 + 0.8. Throughout this work, we adopt a source distance of 10 kpc, which is consistent with the different distance estimates between 6.7 kpc (Zhou et al. 2020) and 12.5 kpc (Kothes et al. 2018) in the literature.

Radio observations

The radio burst from SGR 1935 + 2154 was detected independently by CHIME at 400–800 MHz and STARE2 at 1.4 GHz (Bochenek et al. 2020; CHIME/FRB Collaboration 2020). The CHIME burst consists of two sub bursts with widths of ∼5 ms separated by ∼30 ms, whereas the STARE2 burst has a single narrow spike with a width of 0.61 ms. According to the total fluence reported by STARE2, the radiated energy (isotropic equivalent) is estimated to be $E^{\rm iso}_{\rm radio} = (0.3\text{–}2.4) \times 10^{35}\,(d/10\,{\rm kpc})^2$ erg. The observed dispersion measures (DM) in both radio observations are consistent with a single value, DM $\sim 332.7\,{\rm pc\,cm^{-3}}$(Bochenek et al. 2020; CHIME/FRB Collaboration 2020), which is in agreement with sources in the Galactic plane. Except for the detection of other low-luminosity radio events,[1] the FAST set stringent upper limits on the radio flux associated with many other X-ray bursts (Lin et al. 2020).

X-ray observations

There are four codetections of the hard X-ray burst associated with the FRB-like radio burst (Mereghetti et al. 2020; Li et al. 2021a; Ridnaia et al. 2021; Tavani et al. 2021). The total duration of the burst is roughly 0.3–0.5 s. The X-ray light curves consist of a few narrow peaks with each sub-burst width $\lesssim$ 10 ms (Mereghetti et al. 2020; Li et al. 2021a; Ridnaia et al. 2021), which is coincident with the radio-burst arrival times (see below). The X-ray spectrum extends up to 250 keV (Li et al. 2021a; Ridnaia et al. 2021) and is fitted by an exponentially-cutoff power law (CPL) function with a typical peak energy $\epsilon_{\rm p} \sim$ 50–100 keV. This is unusually hard compared to other X-ray bursts with comparable (or even higher) fluence detected in the same (Younes et al. 2021) and past (Mereghetti et al. 2020; Li et al. 2021a; Ridnaia et al. 2021) bursting episodes. There is evidence for a temporal spectral hardening associated with two peaks of the burst (Mereghetti et al. 2020; Li et al. 2021a). The isotropic energy in the X-ray bands is $E^{\rm iso}_{\rm X} = (0.5-1.2) \times 10^{40}\,(d/10\,{\rm kpc})^2$ erg, which is $\sim 10^5$ times larger than the radio bands.

Burst arrival time

The arrival time delay of a pulse with an observed frequency of ν with respect to a reference frequency $\nu_{\rm ref}$ is

$$t_{\rm DM}(\nu, \nu_{\rm ref}) = k_{\rm DM} \left(\frac{1}{\nu^2} - \frac{1}{\nu^2_{\rm ref}} \right) {\rm DM}, \quad (1)$$

where $k_{\rm DM} \equiv e^2/(2\pi m_e c) \simeq 4.15\,{\rm ms\,pc^{-1}\,cm^3\,GHz^2}$ is the dispersion constant. The dispersion delay between CHIME and STARE2 is $t_{\rm DM}(600\,{\rm MHz}, 1.53\,{\rm GHz}) \simeq 3.25$ s, which is consistent with the observed time delay between the second CHIME sub burst and the STARE2 burst (see Fig. 1). In fact, the spectrum of the second CHIME sub burst extends up to higher frequency (∼800 MHz), whereas the first CHIME sub burst has an apparent spectral cutoff at $\lesssim$ 600 MHz (CHIME/FRB Collaboration 2020). Furthermore, the spiky temporal structure of the second CHIME sub burst resembles

[1] Most recently, a pair of four-orders-of-magnitude less bright (112 Jy ms and 22 Jy ms) radio bursts with temporal separation of 1.4 s at 1.32 GHz has been discovered by a coordinated multi-telescope observation (Kirsten et al. 2021), albeit without X-ray (or gamma-ray) counterparts.

Table 1. Properties of the radio and hard X-ray burst associated with Galactic magnetar SGR 1935 + 2154 on 2020 April 28.

Band	Telescope	Frequency	Arrival time UT ($\nu_{\rm ref}$)[a]	Total duration	Total fluence	Ref.[b]	Energy[c]
Radio	CHIME	0.4–0.8 GHz	14:34:28.264 (0.6 GHz) 14:34:24.428 (∞)	40 ms[d]	700^{+700}_{-350} kJy ms	(1)	3×10^{34} erg
	STARE2	1.28–1.53 GHz	14:34:25.046 (1.53 GHz) 14:34:24.455 (∞)	0.61 ms[e]	$1.5^{+0.3}_{-0.3}$ MJy ms	(2)	2.4×10^{35} erg
X/γ	Insight-HXMT	1–250 keV	14:34:24.429(2) (∞)[f]	$\sim$0.5 s	$7.1^{+0.4}_{-0.4} \times 10^{-7}$ erg cm^{-2}	(3)	6×10^{39} erg
	Konus-*Wind*	20–500 keV	14:34:24.428(1) (∞)[e]	$\sim$0.3 s	$9.7^{+1.1}_{-1.1} \times 10^{-7}$ erg cm^{-2}	(4)	1.2×10^{40} erg
	INTEGRAL	20–200 keV	14:34:24.434 (∞)[e]	$\sim$0.3 s	$5.2^{+0.4}_{-0.4} \times 10^{-7}$erg cm^{-2}	(5)	5×10^{39} erg
	AGILE	18–60 keV	14:34:24.4 (∞)	$\lesssim$ 0.5 s	5×10^{-7} erg cm^{-2}	(6)	5.6×10^{39} erg

Note.[a]Geocentric arrival time of the first peak at reference frequency $\nu = \nu_{\rm ref}$ with DM = 332.7 pc cm^{-3}; [b](1) CHIME/FRB Collaboration (2020) (2) Bochenek et al. (2020) (3) Li et al. (2021a) (4) Ridnaia et al. (2021) (5) Mereghetti et al. (2020) (6) Tavani et al. (2021); [c]Assuming a distance of 10 kpc; [d]The event consists of two sub bursts with widths of ~5 ms separated by ~30 ms; [e]A single spiky burst; [f]Bursts have complicated temporal structure with multiple narrow peaks and here the geocentric arrival time of the first peak is shown

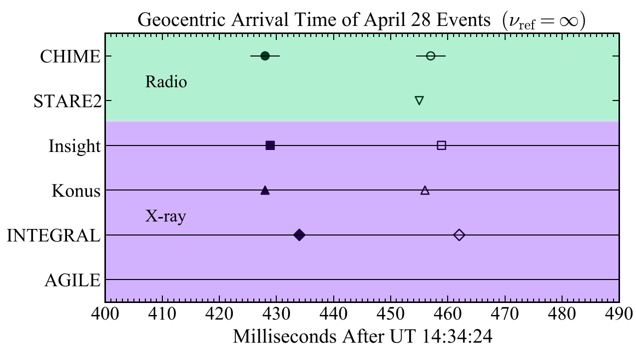

Figure 1. Timelines of the radio and X-ray burst from SGR 1935 + 2154 on 2020 May 28 . The arrival time delay due to radio dispersion is subtracted assuming DM = 332.7 pc cm^{-3} and $\nu_{\rm ref} = \infty$ [see equation (1)]. Each horizontal black bar represents the duration of individual burst. Peak information for AGILE is not available due to the relatively low temporal resolution of ~0.5 s, and not shown here.

that of STARE2 burst. These all implies that the STARE2 burst may be of the same origin as the second CHIME sub burst.

On the other hand, the dispersion delay between CHIME and the X-ray satellites is $t_{\rm DM}(600\,{\rm MHz}, \infty) \sim 3.84$ s. Given this, the arrival times of first/second CHIME sub bursts and the first/second peaks in the X-ray light curves[2] are consistent within error of $\Delta t_{\rm CHIME,\,X} \equiv t_{\rm X} - t_{\rm CHIME} \lesssim 5$ ms. Even if we additionally take into account the finite time resolution of X-ray detectors ($\lesssim 2$ ms around burst peaks) and pulse width of CHIME sub bursts (~5 ms), most conservatively we get $\Delta t_{\rm CHIME,\,X} \equiv t_{\rm X} - t_{\rm CHIME} \lesssim 10$ ms. Similarly, we obtain $\Delta t_{\rm STARE2,\,X} \equiv t_{\rm X} - t_{\rm STARE2} \lesssim 10$ ms for the STARE2 burst and the X-ray second peak. In summary, the intrinsic time separation between X-ray and radio emission peaks is estimated to be no longer than $|\Delta t_{\rm X,\,radio}| \sim 10$ ms.

3 THEORETICAL FRAMEWORK

Whatever the emission mechanism of the the radio burst is, (i) the event is likely to be triggered by an injection of energy into the magnetosphere, and (ii) the radio emission may arise from a relativistic outflow at a sufficiently large distance from the NS surface in order to avoid a significant scattering and absorption. The launch of a relativistic outflow might be accompanied by the formation of a trapped FB (Thompson & Duncan 1995). We first constrain the energy and size of the trapped FB from the X-ray data, and then calculate the expansion of the outflow, assuming that the energy and size of the outflow at launch are comparable to those of the trapped FB.

[2]After the refined analysis, the Integral light curve shows three narrow peaks (Mereghetti et al. 2020). The third peak separated from the second one by ~31 ms is not shown in Fig. 1.

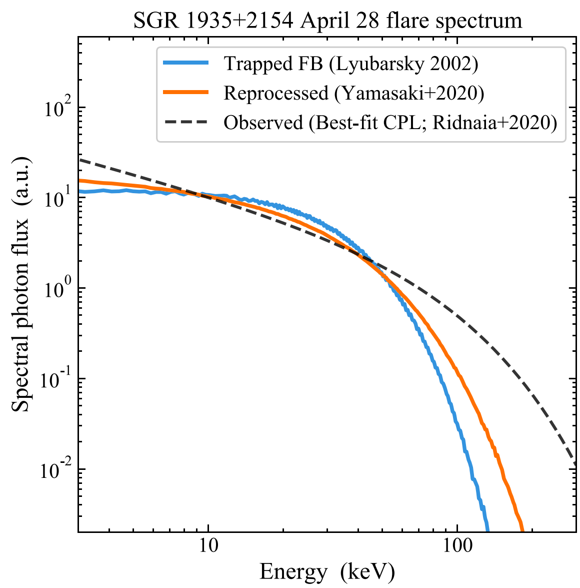

Figure 2. Resonant cyclotron scattering spectra that might be sampled during magnetar flares (Yamasaki et al. 2020, orange solid line). The seed photon spectrum (the modified BB spectrum proposed by Lyubarsky 2002) with an effective temperature of 10 keV is also shown by the blue solid line. The best-fitting exponentially-CPL function $\{dN/d\epsilon \propto \epsilon^{\alpha}\exp[-(\alpha+2)(\epsilon/\epsilon_{\rm p})]$ with $\alpha = -0.72^{+0.47}_{-0.46}$ and $\epsilon_{\rm p} = 85^{+15}_{-10}$ keV$\}$ to the April 28 event obtained by Konus–Wind (Ridnaia et al. 2021) is overplotted with the black dashed line. Spectra are normalized at 10 keV in arbitrary units.

3.1 Trapped fireball

Despite the peculiar light curve and unusually hard spectra of the X-ray burst (Section 2), it is possible that there might be an underlying trapped FB, partially contributing to the thermal part of the entire X-ray burst spectrum. Fig. 2 compares the best-fitting model of observed hard X-ray spectrum (Ridnaia et al. 2021) with the predicted spectra from the trapped FB emission (Lyubarsky 2002; Yamasaki et al. 2020) with an effective temperature of $T_{\rm obs} \sim 10$ keV, which is consistent with the blackbody (BB) plus power-law spectral fitting result with a temperature of $\sim$11 keV (Li et al. 2021a). One can clearly see that the thermal component of the observed spectra could be roughly described by these models (the excess in the non-thermal component will be discussed later in this section). Therefore, we assume that the thermal component of the X-ray burst spectrum might be interpreted as radiation from a trapped FB with a peak photon energy of $\epsilon_{\rm obs} \approx 3T_{\rm obs} \sim 30$ keV, where a factor of 3 reflects the Wien's displacement law.

In the presence of a very strong magnetic field exceeding the critical quantum value $B_{\rm cr} \equiv m_e^2c^3/(e\hbar) \simeq 4.4 \times 10^{13}$ G, the magnetic equilibrium pair number density is expressed as (Canuto & Ventura 1977)

$$n_{\rm e,eq}^{\rm mag}(T) \approx \frac{1}{\sqrt{2\pi^3}}\lambda_{\rm C}^{-3}\frac{B}{B_{\rm cr}}\left(\frac{T}{m_ec^2}\right)^{1/2} e^{-m_ec^2/T}, \quad (2)$$

where $\lambda_{\rm C} = \hbar/(m_ec)$ is the electron Compton wavelength and the numerical factor $(2\pi^3)^{-1/2}\lambda_C^{-3} \simeq 8.1 \times 10^{29}$ cm^{-3}. The energy transfer of the trapped FB under the strong magnetic field is governed by extraordinary-mode (X-mode) photons (Thompson & Duncan 1995; Lyubarsky 2002) with an effective Compton scattering cross section (Meszaros 1992)

$$\sigma_{\rm eff}(\epsilon) = \sigma_T\left(\frac{\epsilon}{m_ec^2}\right)^2\left(\frac{B}{B_{\rm cr}}\right)^{-2}, \quad (3)$$

where ϵ is the X-mode photon energy. The emergent spectrum is determined by the radiation spectrum at the depth corresponding to the mean-free path of an X-mode photon

$$l(T,\epsilon) \sim \frac{1}{n_{\rm e,eq}^{\rm mag}(T)\,\sigma_{\rm eff}(\epsilon)}. \quad (4)$$

By solving the energy transfer equations across the trapped FB, Lyubarsky (2002) found that the emergent spectrum is well approximated by a modified BB with an effective temperature $T_{\rm obs}$. Because of the photon energy dependence of the X-mode cross section [equation (3)], only the Wein part of the BB spectrum with temperature T_0 is effectively observable as an outgoing radiation with temperature $T_{\rm obs}$, and therefore in general $T_0 > T_{\rm obs}$. For simplicity, let us consider an effective X-mode photosphere with a radius R_0 and a uniform background FB temperature T_0, emitting a radiation with a photon energy of $\epsilon_{\rm obs} = 30$ keV. Assuming a uniform magnetic field of $B = B_p$, the mean-free path for X-mode photons is $l(T_0, \epsilon_{\rm obs}) \lesssim \mathcal{O}(1)$ cm for $T_0/m_ec^2 \gtrsim 0.1$, which is vanishingly small compared to the expected FB size R_0.

In the above simple picture (Thompson & Duncan 1995, 1996; Lyubarsky 2002), the total energy of the trapped FB is dominated by the hot plasma component with radius R_0 and temperature T_0 as

$$E_{\rm X,obs} = \frac{4}{3}\pi R_0^3\, aT_0^4, \quad (5)$$

where a is the radiation constant. Meanwhile, the photon diffusion occurs only at the outermost surface with the observed luminosity

$$L_{\rm X} = 4\pi cR_0^2\, aT_{\rm obs}^4. \quad (6)$$

Combining equations (5) and (6), the observed duration of the X-ray emission from the trapped FB is estimated as

$$t_{\rm X,obs} \sim \frac{E_{\rm X,obs}}{L_{\rm X}}. \quad (7)$$

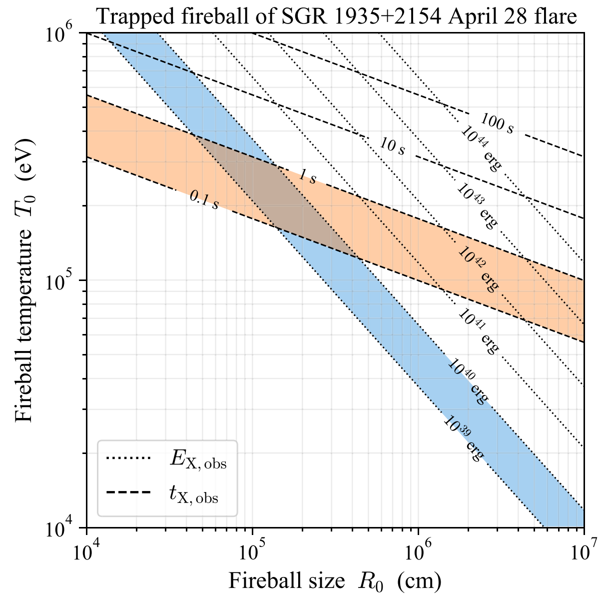

Figure 3. The estimated radius versus temperature of trapped FB for SGR 1935 + 2154 (colored regions), assuming the observed photon energy of $\epsilon_{\rm obs} = 30$ keV. The dotted and dashed lines represent the contours for the observed energy and duration, respectively.

Fig. 3 shows the constrains on the trapped FB parameters. If we conservatively take $E_{\rm X,\,obs} = 10^{39}$–$10^{40}$ erg and $t_{\rm X,\,obs} = 0.1$–1 s, the allowed parameter space for the FB radius and temperature are $R_0 \sim 10^5$ cm and $T_0 \sim 200$–300 keV, respectively. With a BB temperature of 200–300 keV, a good fraction (70 per cent–87 per cent) of the total energy is carried by photons with $\epsilon > m_ec^2$, and hence it is sufficient to keep the interior of trapped FB (except for the thin outer layer) optically thick to pair production. Given the short duration of the emission compared to the spin period $t_{\rm X,\,obs}/P_{\rm spin} \lesssim 0.3$ as well as the relatively small FB size with respect to the NS, the FB may evaporate before being occulted due to the NS rotation.

As mentioned in Section 2, the spectrum of April 28 event is much harder than that of typical bursts from SGR 1935 + 2154 with comparable duration and total energy. The resonant cyclotron scattering may be responsible for the spectral hardening inside flaring magnetosphere. The magnetar magnetosphere is filled with $e^\pm$ plasma both during flares and in the persistent state (Thompson, Lyutikov & Kulkarni 2002; Beloborodov & Thompson 2007; Beloborodov 2013); one can easily see that the resonant cyclotron optical depth is unavoidably large. Therefore any outgoing radiation is reprocessed in the cyclotron resonance layer. In this case, a Doppler shift due to scattering on the bulk motions of the magnetospheric plasma could lead to formation of hard tails in thermal spectra. During the flare, a tremendous resonance radiation force keeps the plasma motion mildly relativistic (Yamasaki et al. 2020). As a result, under typical conditions for flaring magnetosphere, the degree of spectral hardening by a single scattering is at most twice in terms of observed photon energy and the single scattering model can successfully fit the observed intermediate flare (with $L_{\rm X} \sim 10^{40}$–10^{41} erg s^{-1}) spectra from SGR 1900 + 14 (see, e.g. fig. 5 of Yamasaki et al. 2020). Fig. 2 clearly indicates that the predicted spectrum from the trapped FB emission reprocessed by a single resonant cyclotron scattering cannot explain the hard spectral index of April 28 event. Hence, while most spectra of ordinary bursts from SGR 1935 + 2154 might be explained by this model, the formation of the extremely hard spectra of April 28 event by the same picture seems challenging unless one invokes an extremely dense magnetosphere that could lead to multiple resonant scatterings (see also Ioka 2020; Yang & Zhang 2021). Since a further exploration of such a possibility is outside the scope of this work, we just note that magnetospheric reprocession of the trapped FB emission or some alternative mechanisms may give rise to the observed hard X-ray spikes in Section 4.1.

3.2 Relativistic outflow

Next, we consider the relativistic outflows, which might be launched at the onset of the trapped FB formation and produce the radio burst and hard X-ray spikes. The intrinsic energy budget for launching relativistic outflows should be limited by the isotropic equivalent energy emitted by the trapped FB ($E_{\rm X}^{\rm iso} = 10^{40}$ erg). Given the small variability time-scale for radio and X-ray bursts ($\lesssim$ 10 ms), the maximum injected energy available for the outflow would be smaller than $E_{\rm X}^{\rm iso}$. Thus, we conservatively set the initial outflow energy to $E_{\rm flare} \sim 10^{39}$ erg. In addition to the energy and the initial size, the dynamical evolution of the outflow depends on both the composition of the FB and the energy source for acceleration, which are highly uncertain. Thus, we consider a broad class of the outflow models in Section 3.2.1 and discuss its relevance to generation of coherent radio emission in Section 3.2.2.

3.2.1 Outflow models

We consider three outflow models: (i) leptonic outflow composed of $e^{\pm}$ pairs and photons, (ii) baryonic outflow composed of $e^{\pm}$ pairs, baryons, and photons, and (iii) magneto-leptonic (or simply, magnetic) outflow composed of cold $e^{\pm}$ pairs loaded with large Poynting flux. We use the theory of an adiabatic FB (Goodman 1986; Paczynski 1986) to track the dynamical evolution of these outflows (see Appendix A). The evolution of leptonic outflow is uniquely determined for a given set of initial outflow parameters, such as size, temperature, and bulk Lorentz factor (or energy), whereas the latter two outflows are characterized by additional model parameters.

The baryonic outflow is characterized by the baryon loading parameter η defined as a ratio of radiation flux to matter energy flux. The magnetic outflow is described by means of its initial magnetization parameter σ_0 defined as a ratio of Poynting flux to matter energy flux at the magnetosonic point where the outflow attains a velocity of $\Gamma_0 = \sigma_0^{1/2}$ and starts to evolve further[3] (see Appendix for further details). In order to accelerate the magnetic outflow efficiently, a strong dissipation may be important.[4] We adopt a classic model proposed by Drenkhahn 2002 in the context of gamma-ray bursts (GRBs), in which the toroidal magnetic field with alternating polarity (so-called striped wind model; Kennel & Coroniti 1984; Lyubarsky & Kirk 2001) decays into kinetic energy above the light cylinder [$r_{\rm lc} = cP_{\rm spin}/(2\pi) \sim 10^{10}$ cm for SGR 1935 + 2154]. With the assumption that the outflow is highly dominated by magnetic energy and that the thermal energy is negligible, we derive the dynamical evolution at $r > r_{\rm lc}$. We adopt a classic model proposed by Drenkhahn 2002 in the context of GRBs, in which the toroidal magnetic field with alternating polarity (so-called striped wind model; Kennel & Coroniti 1984;

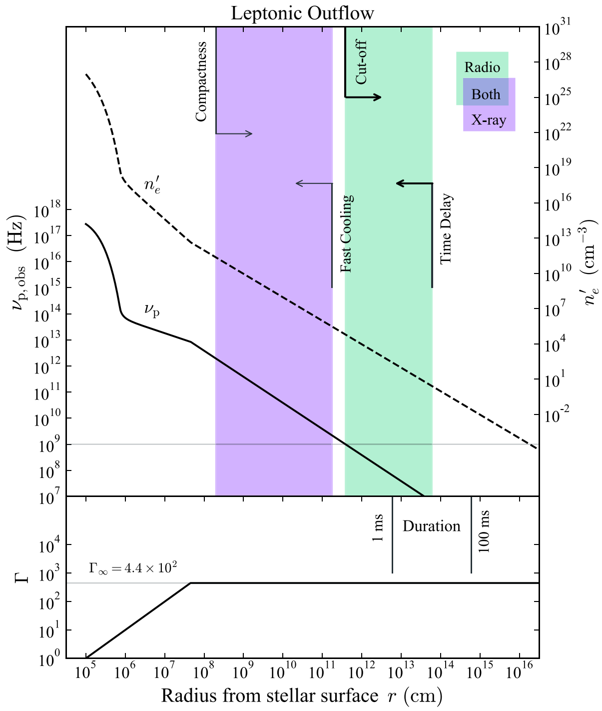

Figure 4. Dynamical evolution of electron number density in the plasma rest frame (upper panel, right-hand-side axis), plasma frequency in the observer frame (upper panel, left-hand-side axis), and bulk Lorentz factor (lower panel) of the leptonic outflow with $E_{\rm flare} = 10^{39}$ erg ($r_0 = 10^5$ cm and T_0 = 200 keV). The allowed radii for X-ray and radio emission are indicated by shaded regions in the upper panel. The region corresponding to the observed burst duration of 1–100 ms is indicated by vertical lines in the lower panel. For radio emission equation (13) and equation (14) are used while for X-ray emission equation (21) and equation (24) are used. We assume $\Delta t_{\rm X,\,radio}$ = 10 ms when deriving the time delay constraints and the duration is evaluated by means of equation (17).

Lyubarsky & Kirk 2001) decays into kinetic energy above the light cylinder [$r_{\rm lc} = cP_{\rm spin}/(2\pi) \sim 10^{10}$ cm for SGR 1935 + 2154]. With the assumption that the outflow is highly dominated by magnetic energy and that the thermal energy is negligible, we derive the dynamical evolution at $r > r_{\rm lc}$.

Based on the trapped FB properties estimated in Section 3.1, we fix the initial non-magnetic outflow radius and temperature to be $r_0 = R_0 \sim 10^5$ cm and $T_0 \sim 200$ keV respectively, so that $E_{\rm flare} = 4/3\pi r_0^3 a T_0^4$. The initial density of non-magnetic outflow is set to the thermal equilibrium value, which only depends on T_0. Meanwhile, the evolution of the magnetic outflow is calculated from $r = r_{\rm lc}$. Since we use the cold approximation, the initial density is determined by equating the initial kinetic energy to $E_{\rm flare}$. The black curves in Figs 4–6 show the dynamical evolution of each outflow. The evolution of leptonic outflow is uniquely determined, whereas for baryonic and magnetic outflows we show the evolution with characteristic values of η and σ_0.To summarize, the terminal bulk Lorentz factor that each outflow attains is

$$\Gamma_\infty \sim \begin{cases} 4.4 \times 10^2\, r_{0,5}^{1/4}\, \hat{\Theta}_0 & \text{(Leptonic)} \\ \min[\eta,\, \eta_{\rm heavy}] & \text{(Baryonic)} \\ \sigma_0^{3/2} + \sigma_0^{1/2} & \text{(Magnetic),} \end{cases} \quad (8)$$

where $\Theta_0 = T_0/m_e c^2$ is the dimensionless initial FB (outflow) temperature and hereafter we use a notation $\hat{\Theta}_0 \equiv \Theta_0/0.4$, corresponding

[3]Note that the definition of σ_0 here is different from the conventional one that defines it when the flow is static ($\Gamma_0 = 1$).

[4]One caveat of models with strong dissipation, however, may be that it is not clear whether a highly ordered magnetic field can be maintained at the FRB generation site in order for the synchrotron maser mechanism to operate.

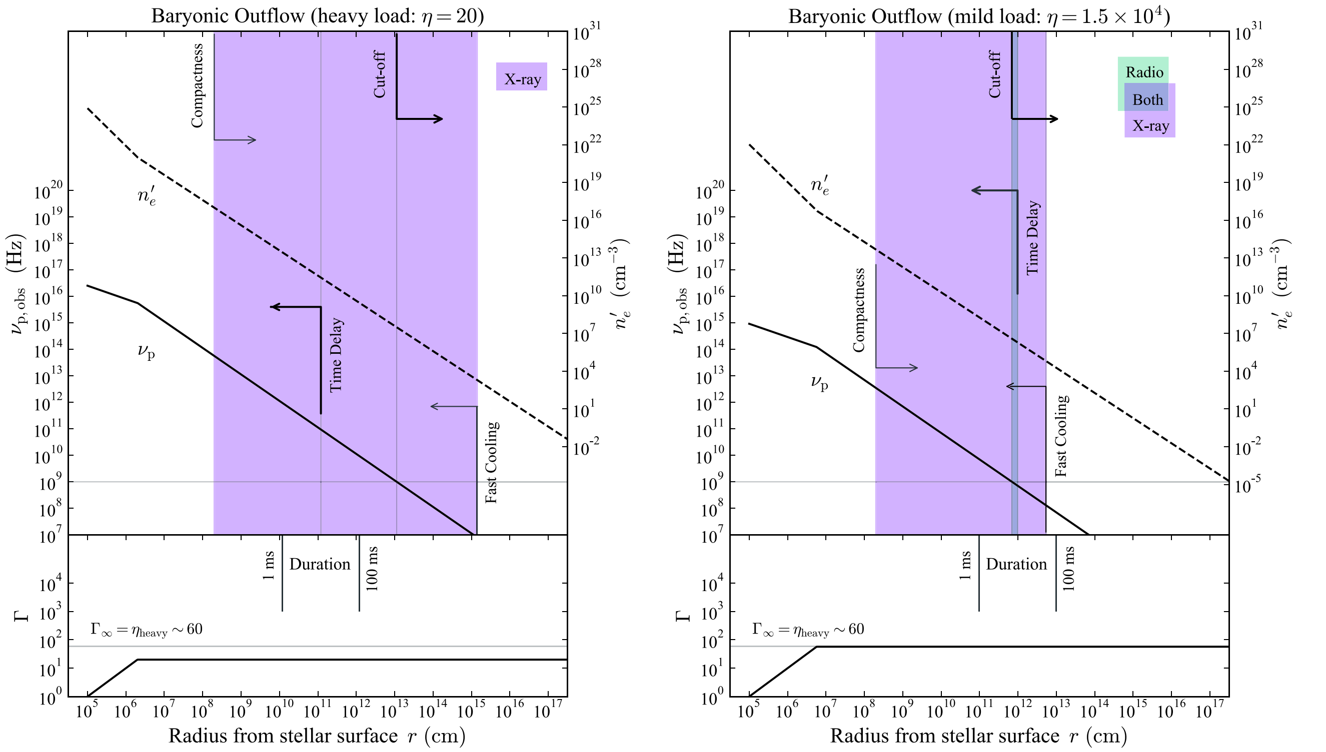

Figure 5. Same as Fig. 4 but for baryonic outflows in the heavy-load $\eta < \eta_{heavy}$ (left) and mild-load $\eta_{heavy} < \eta < \eta_{mild}$ (right) regimes. In the limit of extremely weak baryon load $\eta \to \infty$, the dynamical evolution of the outflow asymptotically approaches to that of a pure leptonic one shown in Fig. 4. Note that the upper limit on the radii due to the fast cooling scales as $\propto \epsilon_B$ [equation (24)] and could be much smaller than shown here (we take an extreme limit $\epsilon_B = 1$), in which case the radio-emitting region may not overlap with the X-ray-emitting region.

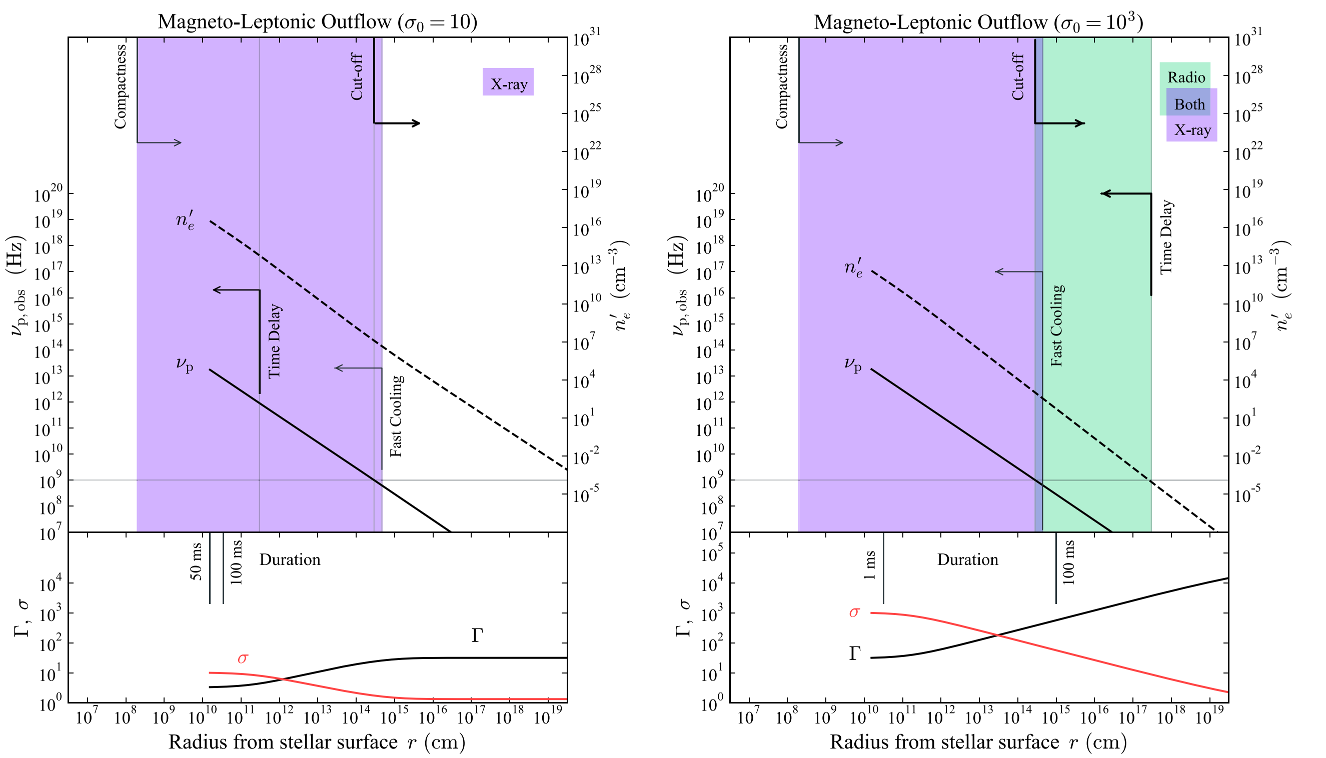

Figure 6. Same as Figs 4 and 5 but for magneto-leptonic outflows with initial degree of magnetizations $\sigma_0 = 10$ (left) and $\sigma_0 = 10^3$ (right). The outflow energy is set to $E_{flare} = 10^{39}$ erg at $r = r_{lc}$. The radial evolution of magnetization parameter σ is also shown in the lower panels.

to $T_0 = 200$ keV. We cover the baryonic outflows in heavy ($\eta < \eta_{\rm heavy}$) and mild ($\eta_{\rm heavy} < \eta < \eta_{\rm mild}$) load regimes, where $\eta_{\rm heavy} \sim 60\, r_{0,5}^{1/4}\, \hat{\Theta}_0$ and $\eta_{\rm mild} \sim 1.5 \times 10^4\, \hat{\Theta}_0\, r_{0,5}$ are the critical values (see Appendix A).

One concern regarding the early evolution of the outflow is the possible disturbance by the large-scale magnetic field of the magnetar. Given a dipole magnetic field $B \propto r^{-3}$, the background magnetic pressure at an altitude h above the NS surface is $P_{\rm B} = B^2/(8\pi) \sim 4 \times 10^{26}\, B_{\rm p,14}^2\, h_6^{-6}$ erg cm^{-3}, whereas the total pressure of the non-magnetic outflow with initial temperature T_0 is $P_{\rm fb} = aT_0^4 \sim 3 \times 10^{23}\, \hat{\Theta}_0^4$ erg cm^{-3}. Namely, $P_{\rm B} \gtrsim P_{\rm fb}$ at an altitude $h \lesssim h_{\rm c} \sim 3 \times 10^6\, B_{\rm p,14}^{1/3}\, \hat{\Theta}_0^{-2/3}$ cm. While a leptonic outflow is barely affected by the background magnetic field because it continues to accelerate up to much larger distance $r_\infty = \Gamma_\infty r_0 \sim 4.4 \times 10^7\, r_{0,5}^{5/4}\, \hat{\Theta}_0$ cm compared to $h_{\rm c}$, it may significantly modify the early evolution of baryonic outflows with low acceleration efficiency $r_\infty \lesssim \eta_{\rm heavy} r_0 \sim 6.0 \times 10^6\, r_{0,5}^{5/4}\, \hat{\Theta}_0$ cm, which is almost comparable to $h_{\rm c}$. In this respect, our estimate on Γ_∞ could be slightly overestimated. The situation might be more complicated for cold magneto-leptonic outflows due to the absence of the radiation pressure. Nevertheless, such uncertainties must be sub-dominant relative to the assumption that the flow starts to evolve at $r = r_{\rm lc}$ with significant acceleration $\Gamma_0 = \sigma_0^{1/2}$. Therefore, we neglect the potential modification of inner outflow evolution by the background magnetic field hereafter.

3.2.2 *Plasma cutoff frequency*

It is often assumed that the GHz coherent emission is generated by coherent charge bunches through, e.g. curvature or synchrotron maser processes. In the case of curvature radiation, the emission is often thought to be triggered by magnetic reconnection in the vicinity of NS (e.g. Katz 2016; Kumar, Lu & Bhattacharya 2017; Ghisellini & Locatelli 2018; Lu & Kumar 2018; Yang & Zhang 2018; Katz 2020; Lu et al. 2020). In the case of the synchrotron maser emission, the emission occurs at relativistic shocks propagating in the pre-existing media, such as nebula (Lyubarsky 2014; Murase, Kashiyama & Mészáros 2016; Waxman 2017), steady magnetar wind (Beloborodov 2017), or past flare-driven ejecta (Metzger, Margalit & Sironi 2019; Beloborodov 2020; Margalit et al. 2020; Yuan et al. 2020; Yu et al. 2021).

In either case, one of the important constraints for localizing the radio emission region comes from the plasma cutoff effect. The waves have cutoff frequencies $\omega_{\rm cutoff}$ (measured in the plasma frame) below which they become evanescent. In general, the cut-off frequency is conveniently expressed in terms of the plasma frequency $\omega_{\rm p}$ defined in the plasma rest frame as

$$\omega_{\rm p} \equiv \zeta \sqrt{\frac{4\pi n_e' e^2}{m_e}}, \tag{9}$$

where n_e' is the comoving number density of electrons in region which is responsible for the generation of waves. We include all the uncertainties associated radiation mechanisms and plasma conditions in the fudge factor ζ, representing both the possible relativistic effects and the specific treatment of the shock. Throughout this work, for simplicity, we set $\zeta = 1$ and leave the parameter dependence to keep generality.

In the case of maser emission at far zone, electromagnetic (EM) waves follow the well-known dispersion relation in the non-magnetized plasma with a cutoff at $\omega_{\rm cutoff} = \omega_{\rm p}$,[5] but the treatment of the shocked region becomes important for an appropriate estimate of plasma frequency. As seen in Section 3.2.1, we calculate the dynamical evolution of a single outflow (Γ and n_e') without deceleration, which may differ from the exact quantitative dynamics of decelerating outflow shells that produce internal shocks. Nevertheless, we can reasonably assume that the most efficient internal shock with a large contrast between shell Lorentz factors and comparable densities is generated at each radius r. We assume that the upstream (downstream) of the shock is cold (hot), and the maser emission is produced by the cold upstream plasma at the shock front. In this case, the apparent plasma frequency in the observer frame for maser-type scenarios is evaluated by (Plotnikov & Sironi 2019, see also Iwamoto et al. 2017, 2019)

$$\omega_{\rm p,obs} \approx \Gamma \omega_{\rm p} \max(1, \sigma^{1/2}), \tag{10}$$

where the coefficient of 3 appearing in the original formula is neglected for simplicity. Here, again, there is an uncertainty in the treatment of bulk Lorentz factor depending on the shock models. But, as this is small $\sim$1, it can be absorbed by the fudge factor ζ in equation (9).

4 CONSTRAINTS ON RELATIVISTIC OUTFLOW AND EMISSION REGION

Based on the outflow models outlined in Section 3.2, we aim to obtain general constraints on the properties of the outflow that is responsible for the generation of radio and hard X-ray bursts from SGR 1935 + 2154.

4.1 Coherent radio burst

Radio emission suffers from various constraints when escaping from the system without significant attenuation, and there is a radio compactness problem when the radio emission originates from relativistic outflows. For example, Murase, Mészáros & Fox (2017) investigated whether radio emission can coincide in region with X-ray and gamma-ray emission in light of FRB 131104 (DeLaunay et al. 2016). Radio waves can propagate only when their frequencies are higher than the plasma cutoff frequency and they also suffer from the induced Compton scattering within the outflows and ambient environments (e.g. Murase et al. 2016). Here, we focus on the plasma cutoff condition for the radio wave propagation:

$$\omega_{\rm p,obs}(r_{\rm radio}) \lesssim \omega_{\rm obs}, \tag{11}$$

[5] In the case of curvature process near the NS, the cyclotron frequency of electrons or positrons $\omega_{\rm B} = eB/(2\pi m_{\rm e} c)$, where B is the local magnetic field strength, is typically much greater than the wave frequency and/or local plasma frequency. In this case (see also Section 3.1), there are two polarization states of EM waves (O-mode and X-mode). While the O-mode wave has the same dispersion relation as in the non-magnetized plasma with a cutoff at $\omega_{\rm cutoff} = \omega_{\rm p}$, the X-mode wave has a complicated dispersion relation with two cutoffs. The lower cutoff lies at $\omega_{\rm cutoff} = (\omega_{\rm p}^2 + \omega_{\rm B}^2/4)^{1/2} - \omega_{\rm B}/2 \sim \omega_{\rm p}^2/\omega_{\rm B}$ when $\omega_{\rm p} \ll \omega_{\rm B}$ (e.g. Chen 1984; Arons & Barnard 1986), indicating $\omega_{\rm cutoff} \ll \omega_{\rm p}$. Depending on how much fraction of the radiation is in X-mode, the condition for the wave propagation may be much more relaxed compared to the non-magnetized plasma case (Kumar et al. 2017). By incorporating this effect, one may estimate the apparent plasma frequency in the observer frame for the curvature-type scenario as $\omega_{\rm p,obs} = \Gamma \omega_{\rm p} \min[(\omega_{\rm obs}'/\omega_{\rm B})^{1/2}, 1]$, where $\omega_{\rm p}$ is estimated by equation (9).

where $\omega_{\rm p,\,obs} = \omega_{\rm p}$ is the apparent plasma frequency in the observer frame. We set the observed radio frequency to $\nu_{\rm obs} = \omega_{\rm obs}/(2\pi) = 1$ GHz in mind of CHIME and STARE2. Depending on the radial evolution of the observed plasma frequency, the above condition sets a limit on the radio-emitting radius $r_{\rm radio}$.

Another constraint comes from the intrinsic timing of radio and X-ray bursts. When there is a bulk motion with a Lorentz factor of Γ, the comoving size of the region responsible for the generation of emission can be larger by a factor of Γ^2. Given the intrinsic time delay $\Delta t_{\rm X,\,radio} \lesssim 10$ ms (see Section 2), the radio (or X-ray) photons should be emitted at

$$r_{\rm radio\,(X)} \lesssim \Gamma^2 c \Delta t_{\rm X,radio} \tag{12}$$

which gives an upper limit on the radio (or X-ray) emitting radius. Since the time delay between X-ray and radio emissions generally depends on the emission mechanisms and initial FB size, it could be much shorter. Also, when there is little or no time delay between X-ray and radio emission as predicted by some models (e.g. Metzger et al. 2019; Margalit et al. 2020; Yuan et al. 2020), the time delay argument [equation (12)] could be less constraining. In this sense, the above limit is most conservative.

Given relativistic outflow models (Section 3.2.1) and maser-type emission (Section 3.2.2), the plasma frequency argument [equation (11)] sets the lower limit on the radio-emitting radius

$$r_{\rm radio} \gtrsim r_{\rm cutoff} \sim \begin{cases} 3.7\times10^{13}\, r_{0,5}^{5/8}\, \hat{\Theta}_0^2\, \zeta\, \nu_{\rm obs,9}^{-1}\ {\rm cm}, & ({\rm L}) \\ 1.1\times10^{13}\, r_{0,5}\, \hat{\Theta}_0^2\, \zeta\, \nu_{\rm obs,9}^{-1} \min[\left(\eta/\eta_{\rm heavy}\right)^{-1/2}, 1]\ {\rm cm} & ({\rm B}) \\ 2.9\times10^{14}\, r_{0,5}^{-1/2}\, E_{\rm flare,39}^{1/2}\, \zeta\, \nu_{\rm obs,9}^{-1}\ {\rm cm} & ({\rm M}), \end{cases} \tag{13}$$

where $r_{\rm cutoff}$ is the plasma cutoff radius defined by $\nu_{\rm p,\,obs}(r_{\rm cutoff}) = \nu_{\rm obs}$. Next, the time delay argument [equation (12)] suggests that the radio emission be emitted at

$$r_{\rm radio} \lesssim \Gamma_\infty^2 c \Delta t_{\rm X,radio} \sim \left(\frac{\Delta t_{\rm X,radio}}{10\ {\rm ms}}\right) \times \begin{cases} 5.8\times10^{13}\, r_{0,5}^{1/2}\, \hat{\Theta}_0^2\ {\rm cm}, & ({\rm L}) \\ 3.0\times10^{14} \min[\eta_3^2, \eta_{\rm heavy,3}^2]\ {\rm cm}, & ({\rm B}) \\ 3.0\times10^{14}\, \sigma_{0,2}^3\ {\rm cm}, & ({\rm M}), \end{cases} \tag{14}$$

which gives an upper limit on the radio-emitting radius. Here, we set $\Gamma = \Gamma_\infty$ to make the radial constraints most conservative.

The allowed region for the radio emission, as well as dynamical evolution, are indicated by the vertical green shaded regions in Figs 4–6. One can see from Fig. 4 that the allowed locale of radio emission from a leptonic outflow is constrained to within somewhat narrow regions at $r_{\rm radio} \sim 10^{12}$–$10^{14}$ cm. On the other hand, the evolution of bulk Lorentz factor of baryonic and magnetic outflows strongly depends on the initial degree of baryon laod (η) and magnetization (σ_0). Figs 5 and 6 demonstrate how these parameters affect the conditions of equation (13) and equation (14). From the left-hand panels of Figs 5 and 6, it is apparent that heavily baryon-loaded and weakly magnetized outflows are not compatible with observed time delay due to the modest acceleration. Meanwhile, although the maximum acceleration is also limited in the the mild-load regime ($\eta_{\rm heavy} < \eta < \eta_{\rm mild}$; the left-hand panel of Fig. 5), there is an allowed range for radio emission site because of smaller plasma frequency. Similarly, the higher initial magnetization σ_0 results in the faster acceleration, which broadens the allowed range of emission region.

As a consequence, the initial properties

$$\eta \gtrsim 6.2\times10^3\, r_{0,5}^{5/4}\, \hat{\Theta}_0\, \zeta^2\, \nu_{\rm obs,9}^{-2} \left(\frac{\Delta t_{\rm X,radio}}{10\ {\rm ms}}\right)^{-2}, \tag{15}$$

$$\sigma_0 \gtrsim 99\, r_{0,5}^{-1/6}\, E_{\rm flare,39}^{1/6}\, \zeta^{1/3}\, \nu_{\rm obs,9}^{-1/3} \left(\frac{\Delta t_{\rm X,radio}}{10\ {\rm ms}}\right)^{-1/3} \tag{16}$$

are required for each outflow to keep the consistency with arguments on the plasma cutoff frequency and the observed time delays between X-ray and radio emission, i.e. $r_{\rm cutoff} \lesssim \Gamma_\infty^2 c\Delta t_{\rm X,radio}$. In equation (16), we use an approximation $\Gamma_\infty = \sigma_0^{3/2} + \sigma_0^{1/2} \sim \sigma_0^{3/2}$ for simplicity.

The observed duration of the burst emission that each outflow predicts can be estimated by

$$\delta t \sim \frac{r}{c\Gamma^2}. \tag{17}$$

Considering the observed duration of interest $\delta t = 1$–100 ms, we show the allowed emission region in the lower panels of Figs 4–6. By examining whether it overlaps with the radio-emitting region, one finds that the leptonic outflow, mildly-loaded baryonic outflow are in principle compatible with radio observations. Meanwhile, heavily baryon-loaded and magnetized outflows cannot reproduce sufficiently short duration of radio bursts due to their weak or delayed acceleration.

4.2 Hard X-ray bursts from relativistic outflow

The existence of non-thermal component in the observed X-ray spectra implies that the source is optically thin to Thomson scattering on $e^\pm$ pairs,[6] which is often the case with the prompt emission of GRBs. An inevitable source for such pairs is the annihilation of photons with rest-frame energy above $m_e c^2$. The scattering optical depth for created pairs is expressed as (Nakar 2007; Matsumoto, Nakar & Piran 2019)

$$\tau_{\rm T} \approx \frac{\sigma_{\rm T} f_{\rm th} N'}{\pi \theta_X^2 r_{\rm X}^2}, \tag{18}$$

where N' is the total number of emitted photons in the rest frame of the outflow and $f_{\rm th}$ the fraction of photons that create pairs. We approximate the energy-averaged cross-section as $\sigma_{\rm T}$ for simplicity. The observer-frame quantities, θ_X and $r_{\rm X}$, are the geometric opening angle (relative to the outflow direction of motion) within which most of the photons propagate and radial distance of X-ray emission region, respectively. The total number of photons is related to observed quantities by $N' \approx (L_{\rm X}^{\rm iso}\delta t_{\rm X}/\epsilon_{\rm p})/\delta_{\rm D}^2(\theta, \Gamma)$, where $L_{\rm X}^{\rm iso}$, $\delta t_{\rm X}$, $\epsilon_{\rm p}$ are the isotropic equivalent X-ray luminosity, the variability time-scale (corresponding to the observed peak width of X-ray burst spikes), and the peak energy of photons in observed νF_ν spectra, respectively. Here $\delta_{\rm D} \equiv 1/[\Gamma(1-\beta\cos\theta)]$ denotes the Doppler factor corresponding to a Lorentz factor Γ (and velocity β) and observer viewing angle θ, which is measured from the center of the X-ray beam. The angular variation of the Doppler factor depends on the product $\Gamma\theta$ and the size of X-ray emission region satisfies: $\theta_{\rm X} \sim \max(1/\Gamma, \theta)$. Generally, the radial distance of X-ray emission region $r_{\rm X}$ is limited by the variability time-scale $\delta t_{\rm X}$. Here, we conservatively assume

$$r_{\rm X} \sim \Gamma\beta\delta_{\rm D}(\theta, \Gamma) c\delta t_{\rm X}, \tag{19}$$

[6] Since the maximum observed photon energy ∼250 keV (Ridnaia et al. 2021) of the hard X-ray counterpart to the radio burst on April 28 is well below $m_e c^2$, the opacity to $\gamma\gamma$ pair production provides less stringent constraints on the beaming of the outflow.

which is true at least inside the beam with angle $1/\Gamma$ regardless of specific dissipation mechanisms (Piran 1999) and indeed gives the loosest limit on the pair creation optical depth even outside the beam (Matsumoto et al. 2019). The relativistic beaming effect can also significantly change the pair-creation criteria and we define the energy threshold of photons which can self-annihilate as $\epsilon_{\rm th} = \delta_{\rm D}(\theta, \Gamma) m_e c^2$ (Lithwick & Sari 2001). Then, the number fraction of annihilating photons in equation (18) is estimated by

$$f_{\rm th} = \int_{\epsilon_{\rm th}}^{\infty} \frac{{\rm d}N}{{\rm d}\epsilon} {\rm d}\epsilon, \tag{20}$$

where ${\rm d}N/{\rm d}\epsilon$ is the observed photon flux normalized to unity. The hard X-ray spectrum of FRB 200428 extends up to 250 keV and is fitted by an exponentially-CPL function ${\rm d}N/{\rm d}\epsilon \propto \epsilon^{\alpha} \exp[-(\alpha+2)(\epsilon/\epsilon_{\rm p})]$ with $\alpha = -0.72^{+0.47}_{-0.46}$ and $\epsilon_{\rm p} = 85^{+15}_{-10}$ keV (Ridnaia et al. 2021). Additionally, we take $L_{\rm X}^{\rm iso} \sim 10^{41}$ erg s^{-1} and $\delta t_{\rm X} \sim 10$ ms for the hard X-ray burst, so that isotropic energy is consistent with the total outflow energy $E_{\rm flare} \sim 10^{39}$ erg.

Then, the requirement that $\tau_{\rm T} < 1$ leads to the limit on observer viewing angle θ, Lorentz factor Γ, and the radial distance $r_{\rm X}$ at which the X-ray emission escapes from the relativistic outflow. We find that the resulting constraints on the Lorentz factor and beaming are rather weak: $\theta \lesssim 0.8$ and $\Gamma \gtrsim 1$, which is largely due to the much lower peak energy and luminosity with respect to those of GRBs. Nevertheless, one can set a generic limit on the radius above which non-thermal emission can be produced as

$$r_{\rm X} \gtrsim 2 \times 10^{8}\ L_{\rm X,41}^{\rm iso 1/2} \delta t_{\rm X,-2}^{1/2}\ {\rm cm}, \tag{21}$$

which is independent of outflow models presented in Section 3.2.

Provided that the hard X-ray burst is synchrotron emission, the large flux of X-rays may ensure that X-ray emitting electrons would be in fast cooling regime regardless of its origins. For non-magnetic outflows, we assume that a fraction ϵ_B of the total internal energy density of the outflow is converted into magnetic energy in the frame of shocked fluid as $B'^2 \approx 8\pi\epsilon_B \Gamma^2 U'$, where $U' = m_e n'_e c^2$ is the internal energy density of upstream material. For magnetic outflow, we can directly determine the magnetic field behind the shock as $B'^2 \approx 4\pi\sigma\Gamma^2 U'$. The synchrotron cooling Lorentz factor of outflow material is given by (Sari, Piran & Narayan 1998)

$$\gamma_c = \frac{6\pi m_e c}{\sigma_T B'^2 \Gamma t}, \tag{22}$$

where $t \sim r/(\Gamma^2 c)$ is the dynamical time-scale of the flow in the frame of the observer. The typical Lorentz factor of electrons at the internal shock may be estimated by assuming that a fraction ϵ_e of the total internal energy goes into random motions of the electrons:

$$\gamma_{\rm m} \sim \epsilon_e \xi_e^{-1} \Gamma, \tag{23}$$

where $m_e/m_p \le \xi_e \le 1$ is the fraction of electrons that undergo acceleration (Eichler & Waxman 2005). Here, we take $\xi_e = 1$, considering the maximum acceleration expected for an internal shock inside the (magneto-)leptonic outflow. Meanwhile, for baryonic outflow, we choose $\xi_e = 10^{-3}$, which may hold unless the flow is only weakly loaded with baryons ($\eta \gtrsim \eta_{\rm mild} \sim 10^4$). Comparing the dynamical evolution of $\gamma_{\rm c}$ with $\gamma_{\rm m}$, one can show that the outflow is in fast-cooling regime ($\gamma_{\rm m} > \gamma_{\rm c}$) at

$$r_{\rm X} \lesssim \epsilon_e \times \begin{cases} 1.8 \times 10^{11}\ r_{0,5}^2\, \hat{\Theta}_0^2\, \epsilon_{\rm B}\, \xi_e^{-1}\ {\rm cm} & {\rm (L)} \\ 1.4 \times 10^{15}\ r_{0,5}^2\, \hat{\Theta}_0^4\, \epsilon_{\rm B}\, \xi_{e,-3}^{-1} \min[(\eta/\eta_{\rm heavy})^{-1}, 1]\ {\rm cm} & {\rm (B)} \\ 4.7 \times 10^{14}\ r_{0,5}^{-1}\, E_{\rm flare,39}\, \xi_e^{-1}\ {\rm cm} & {\rm (M)}, \end{cases} \tag{24}$$

where we have used an analytic expression for the evolution of magnetic outflow (see Appendix A). Hence, this could be considered as an upper limit on the X-ray emission radius. Clearly, the leptonic outflow cannot keep a high radiation efficiency far outside the magnetosphere. In equation (24), the possible uncertainty stemming from the treatment of bulk Lorentz factor used in equations (22) and (23), which depends on the detail of the shock model is neglected here.

By combining the available constraints on X-ray and radio emission with the duration constraint [equation (17)], one finds that the leptonic outflow is excluded since it is unable to explain the X-ray burst duration. Due to the same reason, mildly-loaded baryonic outflows is also excluded. In contrast to the non-magnetic cases, high-σ_0 flows are marginally consistent with observations, albeit with somewhat long duration (>10 ms) for radio emission.

5 SUMMARY AND DISCUSSION

In this work, we constrained the outflow properties associated with the unique April 28 event from SGR 1935 + 2154 consisting of radio and X-ray bursts. The event is likely to be triggered by sudden eruptions of magnetic energy of $\sim 10^{39}$–10^{40} erg into the magnetosphere, which would generate FB plasmas. As a consequence, a relativistic outflow might be launched at the onset of the trapped FB formation. In this case, the hard X-ray burst can be explained as a mixture of thermal and non-thermal emission. We showed that the thermal component of the X-ray burst spectrum is consistent with a trapped FB with temperature of a few hundred keV and size of $\sim 10^5$ cm.

On the other hand, non-thermal radiation, including the non-thermal component of X-ray burst and the coherent radio burst, may arise from the relativistic outflow at large distances from NS ($r_{\rm X} \sim 10^8$–10^{10} cm and $r_{\rm radio} \gtrsim 10^{11}$–$10^{12}$ cm) to avoid absorption/scattering by the outflow itself. We calculated the dynamical evolution of the outflow so that its initial conditions are consistent with the inferred properties of the trapped FB. By assuming that these emissions are both produced by the energy dissipation at the internal shocks of the outflow, we show that any outflows should be accelerated up to bulk Lorentz factor of order $\sim 10^2$ at the outer edge of magnetosphere.

Furthermore, by examining the intrinsic timing offset between radio and X-ray burst spikes with $\lesssim 10$ ms, we constrain the initial degree of baryon load and magnetization, showing that $\eta \gtrsim 6 \times 10^3$ and $\sigma_0 \gtrsim 100$, respectively. The former constraint translates into an upper limit on the total baryon mass of $m_b \lesssim 1.8 \times 10^{14}$ g, which is many orders of magnitude smaller than that inferred from the afterglow observation of historical giant flare from SGR 1806–20: $m_b \sim 10^{20}$–10^{23} g (Nakar, Piran & Sari 2005) or $m_b \gtrsim 10^{24}$ g (Granot et al. 2006). A more precise time coincidence between the radio and the X-ray burst spikes (say $\Delta t_{\rm X,\,radio} \lesssim 1$ ms), if confirmed by a joint radio-X-ray timing analysis, would place stringent constraints on the baryon load and initial magnetization of the outflow. We defer the investigations of more realistic but complicated outflow models that include both baryons and magnetization within the GRB context (e.g. Gao & Zhang 2015) for future works.

Our results may have important implications for why the hard X-ray burst and coherent radio burst seen in April 27 event is rarely observed. An interesting possibility is that magnetar flares launch relativistic outflows with different properties (e.g. degrees of baryon load and magnetization) and/or beaming (e.g. Lin et al. 2020; Zhang 2021). In this case, the radiative efficiency changes from burst to burst. For example, one can speculate that the April 27 event might have loaded baryons. Correspondingly, the radial regions for fast cooling can be expanded, enabling the hard X-ray emission. The diversity can be expected if ordinary flare events typically launch quasi-leptonic outflows (or even do not launch any outflow).

Finally, we encourage the search for the counterpart emissions at different wavelengths on different time-scales. In the framework of 'burst-in-bubble' model outlined by Murase et al. (2016), relativistic outflows associated with the April 28 event may eventually collide with the nebula, leading to afterglow emission at multi wavelengths. Future searches will be important for probing relativistic outflows with properties constrained by this work.

During finalizing the manuscript, we became aware of Ioka (2020), in which a formation of an extremely optically-thick trapped FB ($T_{\rm obs}$ = 30 keV) near the bottom of open magnetic field lines is considered. This special trapped FB powers an outflow that accelerates along the open magnetic field lines, which would generate the hard X-ray burst through diffusion of the X-mode FB photons. As discussed in Section 3.1, such a scenario might be an interesting alternative to the possibility of generating hard X-ray bursts by multiple resonant scattering of original emission from an ordinary trapped FB ($T_{\rm obs} \sim 10$ keV).

ACKNOWLEDGEMENTS

We thank the anonymous referee for useful comments that improved the manuscript. We also thank Anna Ridnaia for sharing detailed information of the hard X-ray burst detected by Konus-Wind, Yuri Lyubarsky for a useful conversation on the evolution of magnetized outflow and Kunihito Ioka for useful comments on the effect of global magnetic field that can affect the early evolution of the outflow. The work of SY was supported by the Institute for Cosmic Ray Research and the advanced European Research Council (ERC) grant TReX. The work of KK is supported by KAKENHI No. 20K04010. The work of KM is supported by the National Science Foundation (NSF) grant No. AST-1908689, No. AST-2108466, and No. AST-2108467, and KAKENHI No. 20H01901 and No. 20H05852.

DATA AVAILABILITY

This is a theoretical paper that does not involve any new data.

REFERENCES

Arons J., Barnard J. J., 1986, ApJ, 302, 120
Beloborodov A. M., 2013, ApJ, 777, 114
Beloborodov A. M., 2017, ApJ, 843, L26
Beloborodov A. M., 2020, ApJ, 896, 142
Beloborodov A. M., Thompson C., 2007, ApJ, 657, 967
Beskin V. S., Kuznetsova I. V., Rafikov R. R., 1998, MNRAS, 299, 341
Bochenek C. D., Ravi V., Belov K. V., Hallinan G., Kocz J., Kulkarni S. R., McKenna D. L., Nature, 587, 59
Borghese A., Coti Zelati F., Rea N., Esposito P., Israel G. L., Mereghetti S., Tiengo A., 2020, ApJ, 902, L2
Canuto V., Ventura J., 1977, Fundam. Cosm. Phys., 2, 203
Chen F. F., 1984, Introduction to Plasma Physics and controlled fusion, 2nd edition. Plenum Press, New York
CHIME/FRB Collaboration, 2020, Nature, 587, 54
Contopoulos I., Kazanas D., 2002, ApJ, 566, 336
DeLaunay J. J. et al., 2016, ApJ, 832, L1
Drenkhahn G., 2002, A&A, 387, 714
Drenkhahn G., Spruit H. C., 2002, A&A, 391, 1141
Eichler D., Waxman E., 2005, ApJ, 627, 861
Gao H., Zhang B., 2015, ApJ, 801, 103
Ghisellini G., Locatelli N., 2018, A&A, 613, A61
Goodman J., 1986, ApJ, 308, L47
Granot J. et al., 2006, ApJ, 638, 391
Grimsrud O. M., Wasserman I., 1998, MNRAS, 300, 1158
Ioka K., 2020, ApJ, 904, L15
Israel G. L. et al., 2016, MNRAS, 457, 3448
Iwamoto M., Amano T., Hoshino M., Matsumoto Y., 2017, ApJ, 840, 52
Iwamoto M., Amano T., Hoshino M., Matsumoto Y., Niemiec J., Ligorini A., Kobzar O., Pohl M., 2019, ApJ, 883, L35
Katz J. I., 2016, ApJ, 826, 226
Katz J. I., 2020, MNRAS, 499, 2319
Kennel C. F., Coroniti F. V., 1984, ApJ, 283, 710
Kirsten F., Snelders M. P., Jenkins M., Nimmo K., van den Eijnden J., Hessels J. W. T., Gawroński M. P., Yang J., 2021, Nature Astron., 5, 414
Komissarov S. S., Vlahakis N., Königl A., Barkov M. V., 2009, MNRAS, 394, 1182
Kothes R., Sun X., Gaensler B., Reich W., 2018, ApJ, 852, 54
Kumar P., Lu W., Bhattacharya M., 2017, MNRAS, 468, 2726
Li C. K. et al., 2021a, Nature Astron., 5, 378
Li D. et al., 2021b, Nature, 598, 267
Lin L. et al., 2020, Nature, 587, 63
Lithwick Y., Sari R., 2001, ApJ, 555, 540
Lu W., Kumar P., 2018, MNRAS, 477, 2470
Lu W., Kumar P., Zhang B., 2020, MNRAS, 498, 1397
Luo R. et al., 2020, Nature, 586, 693
Lyubarsky Y. E., 2002, MNRAS, 332, 199
Lyubarsky Y., 2014, MNRAS, 442, L9
Lyubarsky Y., 2021, Universe, 7, 56
Lyubarsky Y., Kirk J. G., 2001, ApJ, 547, 437
Lyutikov M., 2020, preprint (arXiv:2006.16029)
Lyutikov M., Popov S., 2020, preprint (arXiv:2005.05093)
Margalit B., Beniamini P., Sridhar N., Metzger B. D., 2020, ApJ, 899, L27
Matsumoto T., Nakar E., Piran T., 2019, MNRAS, 486, 1563
Mereghetti S. et al., 2020, ApJ, 898, L29
Meszaros P., 1992, High-energy radiation from magnetized neutron stars, The University of Chicago Press
Metzger B. D., Margalit B., Sironi L., 2019, MNRAS, 485, 4091
Murase K., Kashiyama K., Mészáros P., 2016, MNRAS, 461, 1498
Murase K., Mészáros P., Fox D. B., 2017, ApJ, 836, L6
Nakar E., 2007, Phys. Rep., 442, 166
Nakar E., Piran T., Sari R., 2005, ApJ, 635, 516
Paczynski B., 1986, ApJ, 308, L43
Piran T., 1999, Phys. Rep., 314, 575
Plotnikov I., Sironi L., 2019, MNRAS, 485, 3816
Ridnaia A. et al., 2021, Nature Astron., 5, 372
Sari R., Piran T., Narayan R., 1998, ApJ, 497, L17
Shemi A., Piran T., 1990, ApJ, 365, L55
Simard D., Ravi V., 2020, ApJ, 899, L21
Tavani M. et al., 2021, Nature Astron., 5, 401
Thompson C., Duncan R. C., 1995, MNRAS, 275, 255
Thompson C., Duncan R. C., 1996, ApJ, 473, 322
Thompson C., Lyutikov M., Kulkarni S. R., 2002, ApJ, 574, 332
Uzdensky D. A., Loureiro N. F., Schekochihin A. A., 2010, Phys. Rev. Lett., 105, 235002
Wadiasingh Z., Chirenti C., 2020, ApJ, 903, L38
Wadiasingh Z., Timokhin A., 2019, ApJ, 879, 4
Wang J.-S., 2020, ApJ, 900, 172
Waxman E., 2017, ApJ, 842, 34
Yamasaki S., Kisaka S., Terasawa T., Enoto T., 2019, MNRAS, 483, 4175
Yamasaki S., Lyubarsky Y., Granot J., Göğüş E., 2020, MNRAS, 498, 484
Yang Y.-P., Zhang B., 2018, ApJ, 868, 31
Yang Y.-P., Zhang B., 2021, ApJ, 919, 89
Younes G. et al., 2021, Nature Astron., 5, 408
Yuan Y., Beloborodov A. M., Chen A. Y., Levin Y., 2020, ApJ, 900, L21
Yu Y.-W., Zou Y.-C., Dai Z.-G., Yu W.-F., 2021, MNRAS, 500, 2704
Zhang B., 2021, ApJ, 907, L17
Zhou P., Zhou X., Chen Y., Wang J.-S., Vink J., Wang Y., 2020, ApJ, 905, 99

APPENDIX A: RELATIVISTIC OUTFLOW MODELS

A1 Leptonic wind

First, let us consider an outflow composed of $e^{\pm}$ pairs plus photons. In order to track the evolution of pure-leptonic FB, we follow the formulation by Grimsrud & Wasserman (1998) who considered non-equilibrium effects that would modify the early pair density evolution (see also Appendix of Yamasaki et al. 2019). The conservation of energy, momentum, and pair number density for a steady flow in spherical symmetry leads to a set of simple scaling laws that govern the radial evolution of the bulk Lorentz factor and temperature (Goodman 1986; Paczynski 1986; Shemi & Piran 1990). The bulk Lorentz factor increases linearly with r as $\Gamma \approx \Gamma_0(r/r_0)$ for $r < r_\infty$, where r_0 is the initial FB size and r_∞ the saturation radius above which the acceleration of plasma stops and FB enters a coasting phase with an asymptotic bulk Lorentz factor Γ_∞. Meanwhile the FB temperature cools as $T' \approx T_0(r/r_0)^{-1}$. The dynamical evolution of FB is uniquely determined by initial conditions, i.e. a size r_0, temperature T_0, and Lorentz factor Γ_0. We relate the initial parameters to the total outflow energy $E_{\rm flare}$ by

$$E_{\rm flare} = \Gamma_0 a T_0^4 r_0^3 \sim 10^{40}\, r_{0,5}^3\, \Theta_0^4 \ {\rm erg}, \tag{A1}$$

where we adopt reference values as $r_0 = R_0 \sim 10^5$ cm and $E_{\rm flare} \sim 10^{40}$ erg based on the trapped FB parameters estimated in Section 3.1. In the second equality, we implicitly assume that the initial FB is at rest ($\Gamma_0 = 1$). Note that $\Theta_0 \equiv T_0/m_e c^2$ denotes the dimensionless initial FB (outflow) temperature, which is set to be unity (rather than $\hat{\Theta}_0 = 0.4$ assumed in this work) here for purposes demonstration.

In addition to the dynamical evolution, we consider the evolution of the pair number density, taking into account the interactions among pairs and photons (i.e. creation and annihilation). In the stage of expansion, the FB plasma evolves with the non-magnetic equilibrium number density

$$n_{e,{\rm eq}}(T) \approx \frac{1}{\sqrt{2\pi^3}}\, \lambda_{\rm C}^{-3} \left(\frac{T}{m_e c^2}\right)^{3/2} e^{-m_e c^2/T}. \tag{A2}$$

Compared to equation (2), the magnetic term vanishes and the temperature dependence changes. Starting from $n'_{e,0} = n_{e,{\rm eq}}(T_0)$, the radial evolution of electron (positron) number density is summarized below.

The initial FB is at rest in pair equilibrium due to its high temperature with its size $r = r_0$. It immediately expands and cools down to the electron rest mass energy, and then n_e begins to deviate from $n_{e,{\rm eq}}$. The pair annihilation dominates the pair process since the number of pair-creating high-energy photons decreases as the FB cools. Eventually, the FB reaches the photospheric radius $r_{\rm ph} \sim 2.5 \times 10^6$ cm $r_{0,5}\, \Theta_0$ at which the optical depth to electron scattering becomes an order of unity. When the FB becomes optically thin, photons begin to leak freely out of the photosphere. However, they still continues to supply the radiation energy to pairs, which accelerates pairs up to the coasting radius $r_\infty \sim 1.1 \times 10^8$ cm $r_{0,5}^{5/4}\, \Theta_0$. The photons cease to inject the radiation energy to pairs, and the FB begins to freely coast at constant speed $\Gamma_\infty = r_\infty/r_i \sim 1.1 \times 10^3\, r_{0,5}^{1/4}\, \Theta_0$. At this stage, the pair annihilation no longer occurs due to the small number density. As a result, the total number of pairs conserves and the pair density evolves as $\propto r^{-2}$. The number density of the pair at the coasting phase has an analytical form (Yamasaki et al. 2019):

$$n'_e(r) = 5.5 \times 10^{30}\, r_{0,5}^{3/4}\, \Theta_0^2\, r^{-2} \ \ {\rm cm}^{-3}, \tag{A3}$$

which is valid for $r > r_\infty$. Consequently, the plasma cutoff radius $r_{\rm cutoff}$ at which $\nu_{\rm p}^{\rm maser} = \nu_{\rm obs}$ is

$$r_{\rm cutoff} \sim 2.3 \times 10^{13}\, r_{0,5}^{5/8}\, \Theta_0^2\, \zeta\, \nu_{\rm obs,9}^{-1} \ \ {\rm cm}. \tag{A4}$$

Fig. 4 shows the overall evolution of leptonic FB.

A2 Baryonic wind

Provided that the FB outflow forms in the vicinity of the NS surface, it is expected that some amount of baryons might be contaminated, which was most likely the case for SGR 1806–20 giant flare in 2004 (Granot et al. 2006). This might affect the radial evolution of FB with respect to the pure-leptonic case (e.g. Grimsrud & Wasserman 1998; Nakar et al. 2005). Conservation of baryon number and energy reads

$$\dot{M} = r^2 \rho' \Gamma \beta c = const, \tag{A5}$$

$$L = r^2 (U' + P') \Gamma^2 \beta c = const, \tag{A6}$$

where ρ', U', and P' are the rest mass density, the total energy density, and the total pressure, respectively. In case of baryonic wind, $\rho' = A m_p n'$, where n' is the comoving baryon number density with mass number A (and atomic number Z) and m_p being the proton mass. The magnitude of bulk Lorentz factor is limited by the total entropy per baryon in the FB as

$$\eta \equiv \frac{L}{\dot{M} c^2} = \frac{(U' + P')\Gamma}{A m_p c^2 n'}. \tag{A7}$$

We can see that the adiabatic evolution ($\Gamma \propto r$ and $T' \propto 1/r$) breaks up when the kinetic energy begins to dominate the radiation energy. This transition takes place when $U' + P' \sim A m_p n' c^2$ with a corresponding radius $r_{\rm M} = \eta\, (r_0/\, \Gamma_0)$, above which the Lorentz factor stays constant ($\Gamma_\infty = \eta$). This critical value of η is obtained as

$$\eta_{\rm heavy} \sim 140 \left(\frac{Z}{A}\right)^{1/4} r_{0,5}^{1/4}\, \Gamma_0^{3/4}\, \Theta_0, \tag{A8}$$

by simply setting $r_{\rm M} = r_{\rm ph}$, where the Thomson optical depth is approximated as $\tau_{\rm T} \approx Z n' \sigma_{\rm T} r/\Gamma$, taking into account baryon-associated electrons. An outflow with $\eta \gtrsim \eta_{\rm c}$ becomes optically thin before reaching coasting radius (i.e. $r_{\rm M} < r_{\rm ph}$), the coasting Lorentz factor becomes $\eta_{\rm c}$ at $r > r_{\rm M} = \eta_{\rm c} r_0$. Therefore, the bulk Lorentz factor evolves as

$$\Gamma(r) = \Gamma_0 \begin{cases} r/r_0 & (r < r_{\rm M}) \\ \min(\eta, \eta_{\rm heavy}) & (r > r_{\rm M}), \end{cases} \tag{A9}$$

where $r_{\rm M} = r_0 \min(\eta, \eta_{\rm heavy})$. We consider here the case of relatively high-load FB with $\eta \lesssim 10^4$, for which the number density of positrons becomes negligible compared to that of both electrons and baryons (i.e. $n'_e \sim Z n'$ assuming the charge neutrality). In this case, pair annihilation does not occur anymore and the electron number density conserves:

$$\partial_r \left(r^2 n'_e \Gamma \beta\right) = 0, \tag{A10}$$

where LHS represents the net pair creation rate. Therefore, setting $(U' + P')|_{r=r_0} \sim a T_0^4$ in equation (A7), the radial evolution of the electron number density may be estimated as

$$n'_e(r) \approx \frac{a T_0^4 \Gamma_0}{m_p c^2} \left(\frac{Z}{A}\right) \eta^{-1} \times \begin{cases} (r/r_0)^{-3} & (r < r_{\rm M}) \\ \min(\eta, \eta_{\rm heavy})^{-1}\, (r/r_0)^{-2} & (r > r_{\rm M}). \end{cases} \tag{A11}$$

The above evolution is true up to the second critical point with $\eta = \eta_{\rm mild} \sim 3.8 \times 10^4\,(Z/A)\Theta_0\, r_{0,5}$, when $n'_e \sim Zn'$ at $r = r_{\rm ph}$. The plasma cutoff radius $r_{\rm cutoff}$ at which $\nu_{\rm p} = \nu_{\rm obs}$ is

$$r_{\rm cutoff} \sim 7.1 \times 10^{13}\, r_{0,5}\, \Theta_0^2\, \zeta\, \nu_{\rm obs,9}^{-1}\ \ {\rm cm} \times \begin{cases} 1 & (\eta < \eta_{\rm heavy}) \\ (\eta/\eta_{\rm heavy})^{-1/2} & (\eta_{\rm heavy} < \eta < \eta_{\rm mild}). \end{cases} \quad \text{(A12)}$$

where we assume $\Gamma_0 = 1$ and $Z/A \sim 1$.

Although not covered in this work, for completeness, we briefly describe the weak load case. The weakly-loaded baryonic outflow evolution ($\eta > \eta_{\rm mild}$) can be characterized by the additional critical value of $\eta = \eta_{\rm weak}$ when $m_e n'_e \sim m_p n'$ at $r = r_{\rm ph}$ (hence $\eta_{\rm weak}/\eta_{\rm mild} \sim m_p/m_e$). At $\eta_{\rm mild} < \eta$, the effective electron mass can be approximated as $\tilde{m}_e \approx (A/2Z)m_e\, \min\{\eta_{\rm weak}/\eta, 1\}$ (Nakar et al. 2005). By replacing m_e with $\tilde{m}_e$ in the coasting radius of leptonic outflow $\Gamma_\infty \propto m_e^{-1/4}$, the coasting Lorentz factor Γ_∞ is found to reduce at most by a factor of $(Am_p/2Zm_e)^{1/4} \sim 6\,(A/Z)^{1/4}$ compared to the pure leptonic case. The inequalty between $e^{\pm}$ number density does not significantly change the characteristic radii (e.g. $r_{\rm ph}$) that determine the evolution of a quasi-leptonic outflow throughout $\eta > \eta_{\rm heavy}$ (Grimsrud & Wasserman 1998).

A3 Magneto-leptonic wind

If the central engine carries a strong magnetic field, it may significantly contribute to the energy of the relativistic outflow. We consider a cold magneto-leptonic FB ($P' = 0, U' = \rho' c^2 = n'_e m_e c^2$), corresponding to a relativistic limit with high initial magnetization $\sigma_0 \gg 1$, which is defined by the ratio of Poynting flux to matter energy flux at the magnetosonic point. The total energy and mass flux are linked by

$$L = (1+\sigma)\Gamma \dot{M} c^2, \quad \text{(A13)}$$

where $(1+\sigma)\Gamma$ is a conserved quantity. In Poynting-flux dominated flows, dissipation of magnetic energy can take place via a reconnection process. For non-ideal MHD, the dynamical evolution of outflow in relativistic limit is given by (Drenkhahn 2002; Drenkhahn & Spruit 2002)

$$\partial_r \Gamma = \frac{2}{c\tau_{\rm dis}}\left(\sigma_0^{3/2} + \sigma_0^{1/2} - \Gamma\right), \quad \text{(A14)}$$

where $\tau_{\rm dis}$ is the time-scale for dissipation of toroidal magnetic fields. We assume that the complete field decays into kinetic energy. The time-scale for acceleration is solely determined by specific reconnection processes. Here, we consider an outflow with stripes of a toroidal magnetic field of alternating polarity (e.g. Kennel & Coroniti 1984; Lyubarsky & Kirk 2001). In this case, the dissipation occurs in the outflow outside the light cylinder with lab-frame time-scale

$$\tau_{\rm dis} = \frac{P_{\rm spin}}{\epsilon}\frac{\Gamma^2}{\sqrt{1 - \Gamma/\sigma_0^{3/2}}}, \quad \text{(A15)}$$

where $P_{\rm spin} = 3.24$ s is the spin rate of SGR 935 + 2154 and ϵ is defined as a fraction of advection velocity of magnetic field lines toward reconnection center with respect to Alfvén velocity. Drenkhahn (2002) showed that the Poynting-flux dominated relativistic flow accelerates as $\Gamma \propto r^{1/3}$ up to the coasting value of $\Gamma_\infty = \sigma_0^{3/2} + \sigma_0^{1/2}$ [$\partial_r \Gamma = 0$ in equation (A14)], which is independent of the reconnection rate ϵ. The largest uncertainty lies in the reconnection rate parameter ϵ and we take $\epsilon = 0.1$ as a fiducial value (Drenkhahn 2002). Simulation studies of reconnecting current sheets suggest a smaller value $\epsilon = 0.01$ (e.g. Uzdensky, Loureiro & Schekochihin 2010), which may increase the injection radius by about ten times. Nevertheless, due to the relatively slow acceleration $\Gamma \propto r^{1/3}$, this barely affects our final conclusions.

In the absence of dissipation, the bulk Lorentz factor of a magnetized outflow grows as $\Gamma \approx r/r_{\rm lc}$ due to the balance between the EM and centrifugal forces up to the fast magnetosonic surface, beyond which there is little acceleration (Beskin, Kuznetsova & Rafikov 1998; Contopoulos & Kazanas 2002; Komissarov et al. 2009). We set the initial flow velocity to the Alfvén four-velocity $u_{\rm A} \equiv B'_0/(4\pi\rho'_0 c^2)^{1/2} = \sigma_0^{1/2}$ (where B'_0 is the magnetic field and ρ'_0 is the rest mass density) at the initial radius $r = r_{\rm lc} \sim 10^{10}$ cm. Since the dissipation only sets in at $r_{\rm inj} \sim r_{\rm lc}/\epsilon = 10\epsilon_{-1}^{-1}\, r_{\rm lc}$, we can safely neglect the dynamical evolution before passing the fast magnetosonic point (Drenkhahn 2002), unless an extremely high magnetization ($\sigma_0 \gg 1000$) is considered. The initial pair number density is determined at $r = r_{\rm lc}$ by the following condition:

$$E_{\rm flare} \sim (1+\sigma_0)\Gamma_0^2 4\pi \rho'_0 c^2 r_0\, r_{\rm lc}^2, \quad \text{(A16)}$$

where $\Gamma_0 \approx u_A = \sigma_0^{1/2}$. For a cold magnetized outflow, the pair annihilation is negligible and thus the evolution of pair number density is estimated by equation (A10). For initial magnetizations of $\sigma_0 = 10$–1000, we numerically evaluate the dynamical evolution with equation (A14) and obtain $r_{\rm cutoff} \sim 10^{13}$–$10^{14}$ cm. For analytic estimate, we use

$$\Gamma \sim \begin{cases} \Gamma_0 & (r_{\rm lc} < r < r_{\rm inj}) \\ \Gamma_0 (r/r_{\rm inj})^{1/3} & (r_{\rm inj} < r < r_{\rm sat}) \\ \Gamma_\infty & (r_{\rm sat} < r), \end{cases} \quad \text{(A17)}$$

where $r_{\rm sat} \sim r_{\rm inj}\Gamma_\infty^2$ (Drenkhahn 2002) is the saturation radius where the acceleration ends. We confirm that this gives a very good approximation of Lorentz factor during the acceleration phase for $\sigma_0 \gg 1$. Assuming that the flow is in the acceleration phase, we obtain the cutoff radius for maser-type emission as

$$r_{\rm cutoff} \sim 2.9 \times 10^{14}\, r_{0,5}^{-1/2}\, E_{\rm flare,39}^{1/2}\, \zeta\, \nu_{\rm obs,9}^{-1}\ \ {\rm cm}, \quad \text{(A18)}$$

which is remarkably independent of σ_0 and ϵ.

This paper has been typeset from a TEX/LATEX file prepared by the author.